Eutectic melting of Fe-3 at% Si-4 at% C up to 200 GPa and implications for the Earth's core

F. Miozzi, G. Morard, Daniele Antonangeli, M.A. Baron, S. Boccato, A. Pakhomova, G. Garbarino, M. Mezouar, G. Fiquet

Eutectic melting of Fe-3at% Si-4at% C up to 200 GPa and implications for the Earth's core.

Miozzi, F.[1,+*], Morard, G.[1,¥], Antonangeli D.[1], Baron, M. A.[1], Boccato, S.[1], Pakhomova, A.[2], Garbarino, G.[3], Mezouar, M.[3] & Fiquet, G.[1]

[1] Sorbonne Université, UMR CNRS 7590, Muséum National d'Histoire Naturelle, Institut de Minéralogie, de Physique des Matériaux et de Cosmochimie, IMPMC, 75005 Paris, France

[2] Deutsches Elektronen-Synchrotron (DESY). Hamburg, Germany

[3]European Synchrotron Radiation Facility (ESRF). Grenoble, France

[+]now at: Dipartimento di Scienze della Terra, Università degli Studi di Milano, via Mangiagalli 34, 20133 Milano, Italy.

[¥]now at: Univ. Grenoble Alpes, Univ. Savoie Mont Blanc, CNRS, IRD, IFSTTAR, ISTerre, 38000 Grenoble, France

*miozzi.f@gmail.com

Highlights

-The iron-rich corner of the ternary phase diagram is defined up to 200 GPa and 3000 K.

-The alloy crystalizes into Fe hcp and Fe_3C with hcp Fe hosting silicon and carbon.

-The eutectic melting temperature of this ternary alloy is lower than Fe-Si and Fe-C.

- Fe-Si-C melting temperature satisfies the constraints for the core mantle boundary.

Abstract

Properties of the Fe-Si and Fe-C binary systems have been shown unable to satisfy the geophysical and petrological constraints of the Earth's core (i.e. velocities, densities, melting temperature) if only Si or C were to be incorporated as light element. Recent *ab initio* calculations suggest on the contrary that density, compressional and shear sound velocities, as well as the Poisson's ratio of the inner core could be matched by an hcp-Fe alloy containing Si and C. The combined effect of the two elements in a ternary Fe-Si-C system has never been experimentally investigated under high pressure. We thus studied the melting curve and the phase relations of the ternary iron-silicon-carbon system by *in situ* X-ray diffraction at high pressures and high temperatures. Starting with a low light element content (4at%C-3at%Si), a stable assemblage made of hcp Fe (+Si, +C) and Fe_3C is observed up to 200 GPa. Fe can incorporate both Si and C in its hexagonal structure, with the latter strongly affecting the volume and the melting temperature. While the presence of a third light element is likely necessary, we here

document that the effect of C in lowering the melting temperature of Fe-Si, is large enough to possibly keep the core-mantle boundary temperature below the solidus of the mantle silicates.

Keywords: light elements, carbon, silicon, core, high pressure, melting,

1. Introduction

Silicon and carbon are listed among the potential light elements alloyed with iron and nickel in the Earth's core, together with sulphur, oxygen and hydrogen (Poirier, 1994). The presence of light elements is advocated since early 60's (Birch, 1964) to reconcile the difference in density between the seismic observations of the Earth's core and an hypothetic pure iron core. To satisfy the seismological observations of the Preliminary Reference Earth Model (PREM) (Dziewonski and Anderson, 1981), the thermo-elastic properties of the iron alloy have indeed to match the density (ρ), longitudinal (V_P) and shear (V_S) wave velocities as a function of depth. In addition, the nature and quantity of light elements have to be compatible with the core-mantle differentiation history and account for the cosmochemical constraints on elemental abundances and/or volatility loss during Earth's accretion (McDonough, 2003). Matching geophysical and geochemical observables is therefore a key approach to understand the Earth's core composition.

In recent years, several studies have been conducted on iron alloyed with Si or C in binary systems (e.g. Fe-Si (Fischer et al., 2013; Lord et al., 2010; Ozawa et al., 2016; Tateno et al., 2015), Fe-C (Mashino et al., 2019; Mookherjee, 2011; Morard et al., 2017; Vočadlo et al., 2000)) and few in the ternary systems(e.g. Fe-Si-Ni (Antonangeli et al., 2010), Fe-Si-S (Tateno et al., 2018)). However a candidate composition satisfying all the constraints is still to be identified.

Si has often been considered as the main candidate light element in the Earth's core. Its affinity with iron under magma ocean conditions opens a wide range of possible solid solutions, with Si incorporation in the forming core, irrespectively of the oxidized or reduced nature of the accreting material (Siebert et al., 2013). Alloying Si with Fe in the Earth's core is also an elegant way to explain why the Mg/Si ratio for the mantle is higher than the one observed in chondrites (Javoy et al., 2010).

However, recent studies pointed out that an hcp-Fe-Si alloy matching inner core density would have too high sound velocities with respect to seismological observations (Edmund et al., 2019). Furthermore, due to its solid-liquid partitioning coefficient close to 1 at 330 GPa (Alfè et al., 2002), Si alone does not provide a satisfactory solution for the observed density jump at inner core boundary. The presence of oxygen is commonly argues on the base of its very strong affinity with the liquid (Alfè et al., 2002).

Carbon has been considered as well as a likely candidate element in the Earth's core (Wood et al., 2013), because of its natural abundance in iron meteorites (Chabot et al., 2006). Carbon strongly influences the melting behaviour of Fe, with a depression of the melting curve of about 110 K/at % at CMB pressure, sufficient to prevent extensive partial melting of silicates at the core mantle boundary even for relatively small amount of C (Morard et al., 2017). Experimental studies on Fe_3C and Fe_7C_3 end-members have shown that carbon reduces shear velocities and the Poisson ratio of pure Fe, approaching values of the inner core (Prescher et al., 2015). However, its high volatility during Earth's differentiation and low silicate/metal partitioning do not support carbon as the main light element in the Earth's core (Dasgupta, 2013).

Thus, incorporation of Si or C leads to changes in properties of the Fe-alloys that make them suitable as core components, although not in a sole binary system with iron. This has often advocated for the addition of a third light element, such as oxygen. However, the simultaneous presence of silicon and oxygen is possibly limited by the progressive exsolution of SiO_2 when cooling a liquid in the Fe-Si-O ternary system (Hirose et al., 2017). Noteworthy, the combined effect of Si and C in the ternary Fe-Si-C system has not yet been investigated experimentally under high pressure and high temperature. A computational study (Li et al., 2018) determined the elastic properties at core conditions for two Fe-Si-C compositions and proposed that an alloy made by Fe-3at% Si-3 at% C could match PREM density and velocities at the temperature of 6500 K. Hence, in this experimental study we aim to study the phase diagram and melting curve of the Fe-Si-C system, and to measure the thermo-elastic properties of the stable solid phases. Such a dataset is required to assess if a suitable core composition for the Earth's core can be found within the Fe-Si-C ternary system.

2. Experimental methods

The starting material ($FeSi_3C_4$ in the text), with a nominal composition of Fe 93 at%, C 4 at%, Si 3 at%, was synthesized at ICMPE (Institute de Chimie et des Matériaux de Paris-Est, Paris, France) by ultra-fast quench method starting from Fe (Neyco F-12734), Si (Wacker) and Fe_3C (Neyco FC-76857/1). Homogeneous Fe liquid alloys were first obtained by induction melting in a water-cooled Cu crucible under He atmosphere. Ribbon specimens of ~25 μm thickness and 20–30 mm width were produced by the planar flow casting technique. The alloys were then re-melted and ejected through a pressurized quartz nozzle on a rotating Cu-base wheel under 1 bar He atmosphere. Composition of the final products was measured using a Cameca SX100 electron microprobe analyser equipped with a cold finger and an O_2 flux at Camparis center-Sorbonne Université. The measured composition for the alloy is 3 (±0.2) at % Si, 4 (±0.4) at% C and 93 (±0.06) at % Fe. Imaging by scanning electron microscopy (SEM) of the sample texture carried out on a Zeiss Ultra 55 scanning electron microscope at IMPMC laboratory confirmed a good homogeneity at the micron scale.

Samples were then prepared for high-pressure experiments by crushing parts of a ribbon and compressing it between two diamonds with a culet of ~ 600 microns, in order to obtain the desired thickness (usually between 5 and 10 microns). Dried grains of KCl were cold pressed into sheets out of which disks of selected diameters were cut by a femto-second laser and stored at 120°C. KCl served not only as pressure transmitting media and thermal insulator but also as a reliable pressure calibrant. KCl-sample-KCl sandwiches were then loaded in a pre-indented rhenium gasket (initially 200 μm thick), with a drilled hole of 120, 70, 35, 25 μm for diamonds with flat culets of 250 μm and bevelled culets of 150/300, 100/300, 70/300-μm diameters respectively. High pressure was generated by membrane-driven Le Toullec-type diamond anvil cells, equipped with tungsten carbide seats designed for diamonds with a conical support (Boehler and De Hantsetters, 2004), providing a maximum 2-theta angle of 70°. High temperature was generated by double-sided YAG laser heating.

The experimental runs were conducted on ID27 beamline at the European Synchrotron radiation facility (ESRF) (Mezouar et al., 2005) and on P02.2 Extreme Conditions Beamline (ECB) at Petra III at

112 the Deutsche Elektronen Syncrotron (DESY) (Liermann et al., 2015). On ID27 at ESRF a
113 monochromatic beam of 33 KeV (λ = 0.3738 Å, Iodine k-edge) was focused on a sample area of less
114 than 3 × 3 μm^2 (full width at half maximum). Exposure time was usually between 10 and 30 s, and the
115 diffraction signal was collected on a MAR CCD detector. Heating was provided by two continuous
116 Nd:YAG fiber lasers (Transverse Electromagnetic Mode (TEM 00) focused over a visible heating spot
117 >20 μm in diameter. Temperature was measured on both sides of the sample before and after the X-ray
118 exposure (only upstream during the exposure), at the centre of the hot spot region. The analysis of the
119 thermal emission was made on a 2 × 2 μm^2 area selected by a pinhole placed at the entrance of the
120 spectrometer. Further details regarding temperature measurement and the uncertainties are provided in
121 Miozzi et al. (2018). Concerning P02.2 at Petra III, a monochromatic beam of 42.65 KeV (λ = 0.2907
122 Å) was focused on a sample area of 6 x 6 μm^2. The diffraction signal was collected on a PerkinElmer
123 detector with an exposure time between 10 and 30 s. Laser heating experiments have been performed
124 with the available off-axis double-sided laser heating setup. Briefly, a laser light from a 100 W
125 Ytterbium fibre laser (1072 nm, IPG Laser GmbH) was split by a polarizing beam splitter into two
126 Gaussian profile beams (upstream and downstream). The heating power of each branch was controlled
127 via a combination of the polarizing cube beam splitter and half-wave plates. The laser beam was focused
128 by a simple plano-convex lens with an effective focal length of 50.2 mm. Typical laser spot size was
129 ~20 μm, full width at half maximum (FWHM). Light emitted from the hot sample was then collected
130 from both sides by a system of mirrors and lenses and guided to the spectrograph entrance slit. The
131 detecting unit consisted of the ICCD iStar detector mounted on a Shamrock spectrograph (SR-303i-A-
132 SIL) from Andor technology. The transfer function of the optical system for temperature measurement
133 was calibrated using a tungsten halogen lamp (OPTEEMA Engineering GMbH, OL-245M-K3) at
134 2200K, 2500, 2900 K. Spectra from hot sample were corrected by the transfer function and used for
135 temperature calculation by fitting procedure to the Planck's law using the software T-Rax by C.
136 Prescher. Every temperature presented here was considered to have an actual error bar of ±150 K, which
137 results from the measurement uncertainties, including temperature gradients, heating instability, and
138 accuracy of the grey body approximation.

For all the experiments, pressure was determined using the thermal EoS of KCl by (Dewaele et al., 2012), assuming the temperature of KCl to be the average between the temperature of the diamond (295 K) and the temperature measured at the surface of the sample (Campbell et al., 2009). Uncertainties in pressure were propagated from uncertainties in the lattice parameter and from uncertainties on the temperature calibration for KCl as in (Miozzi et al., 2018).

For melting experiments, samples were at first compressed to target pressures, and subsequently heated until the melting temperature was reached. The appearance of diffuse scattering contribution to the diffraction pattern (Figure S1) and the plateau in the evolution of measured temperature vs. laser power were used as melting criteria (Lord et al., 2010; Morard et al., 2017). Samples were heated up and quenched after melting by cutting the laser power. The same procedure was repeated on a fresh spot on the sample. In some cases, the very same spot was re-heated at moderate T to induce recrystallization of the quenched sample so as to make *in situ* analysis of the run products by Rietveld refinement of diffraction patterns.

Subsolidus experiments were also carried out to constrain the phase diagram and to collect data in order to establish a P-V-T equation of state. Cycles of heating were done without reaching the melting temperature, up to pressures limited by the stability of diamonds and its culets size. The raw data were processed with Dioptas (Prescher and Prakapenka, 2015) using calibration parameters (sample detector distance and orientation) derived from the diffraction of a cerium dioxide (CeO_2) standard. Each diffraction pattern was indexed and refined with PD Indexer (http://pmsl.planet.sci.kobe-u.ac.jp/~seto/?page_id=20) to obtain the cell parameters of the phases. When possible, the loaded gaskets were recovered after the experiment. Transverse sections of the heating spot (e.g. Figure 1a) were exposed by Ar ion milling and further polished by a focused ion beam (Zeiss Neon40EsB), both available at IMPMC laboratory. Textural analysis of the heating spot was performed to confirm the melting.

3. **Results**

Data were collected for pressures ranging between 20 and 200 GPa and temperatures up to 4000 K. Diffraction patterns of the starting material can be indexed as hexagonal closed packed (hcp) structure. Irrespectively of the pressure, the diffraction rings become well defined and the peaks sharpen upon heating, allowing a precise interpretation of the structures. At high temperature the starting material crystalizes into Si- and C-bearing hcp Fe and Fe_3C indexed with an orthorhombic structure (space group: Pnma) (Liu et al., 2016 and reference therein) (Figure 1b). Carbides peaks appear at T ~ 1500 K at low pressure (P = 50 GPa) and at T ~ 2000 K at high pressure (P = 140 GPa). This is likely related to a kinetic effect, and not to a solubility limit of C and Si in hcp Fe as a function of temperature and pressure. Silicon or silicon-bearing compounds (i.e. SiC, FeSi) were not observed, neither in the diffraction patterns, nor in the transverse cut of the recovered samples. The suit of the collected data allowed us to determine the thermal EoS for both the hcp-Fe (+Si, +C) and the Fe_3C phases, the melting curve and the phase relations at high pressure and temperature.

3.1 Subsolidus phase relations and equations of state

The present study is the first characterisation of subsolidus phase relations in the ternary Fe-Si-C system at pressures higher than a few GPa (Narumi et al., 2014). In particular our dataset describes the iron rich corner of the phase diagram up to 200 GPa. In this study, hcp Fe (+Si, + C) and Fe_3C have been found to be the stable compounds across the entire examined P-T range (Figure 1b). This is in disagreement with the proposed decomposition of Fe_3C into in Fe_7C_3 + Fe above 157 GPa reported by Liu and co-authors (2016), but consistent with the more recent study of the Fe-C binary system carried out by Mashino et al. (2019).

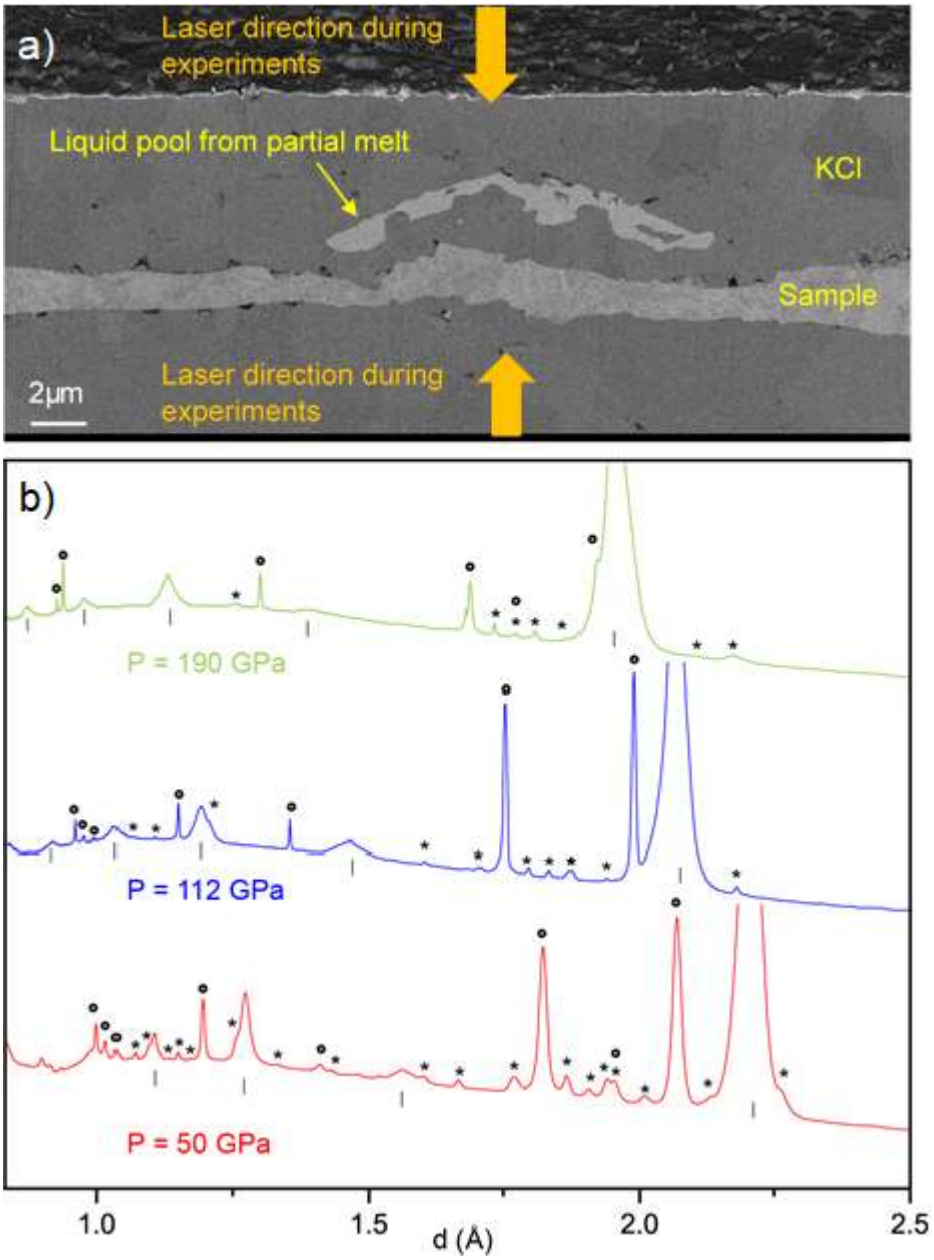

185

186 Figure 1: a) Backscattered electron image of a laser heating spot in $FeSi_3C_4$ cut perpendicular to the
187 laser heating axis. The textured part corresponds to solid part of the sample (typical features from solid
188 metal as in (Morard et al., 2018), whereas the homogeneous part, in arc shape on top, corresponds to
189 the liquid extracted after partial melting. The dark grey areas on both sides of the sample are KCl
190 layers; b) Diffraction patterns collected at 300K on $FeSi_3C_4$ quenched samples showing the
191 coexistence of hcp Fe (+Si, +C) and Fe_3C. Intensity (in arbitrary) units is plotted vs. d-spacings. Stars
192 represent peaks indexed as Fe_3C and circles hcp Fe (+Si, +C), the small ticks stand for KCl.

193

194 Measured volumes of quenched hcp Fe collected in this study are presented in Figure 2 and are
195 systematically larger, over the whole pressure range, than those of pure hcp Fe from literature (e.g.
196 Dewaele et al., 2006; Fei et al., 2016; Miozzi et al., 2020). Although Si shows a large solubility in hcp

Fe under high pressure, up to ~18 at % Si (e.g. Fischer et al., 2012; Tateno et al., 2015)), the here-observed volume increase cannot be solely explained by the presence of silicon. Recently, it has been proven that iron hcp structure can incorporate up to 5 wt % Si (about 9.5 at %) without any significant change of the unit cell volume (Edmund et al., 2019). If the decomposition of the starting material into Fe_3C and Fe hcp follows the lever rule (inset in Figure 2), the content of Si in hcp iron is expected to be lower than 9.5 at%. Thus, no volume change should be observed as a consequence of the only Si incorporation. We can then conclude that a small amount of carbon has to be incorporated together with silicon, in order to explain the volume increment of the hcp unit cell, here after called hcp Fe (+Si, +C). Furthermore, the simultaneous presence of Fe_3C with hcp Fe (+Si, +C) suggests that the solubility limit of carbon was reached. The strong effect of small amount of C on the volume of hcp Fe can be related with its interstitial position in the hcp structure (Caracas, 2017; Li et al., 2018). Conversely, Si is incorporated as substitution to iron atoms and therefore does not introduce major changes in the volume (Edmund et al., 2019).

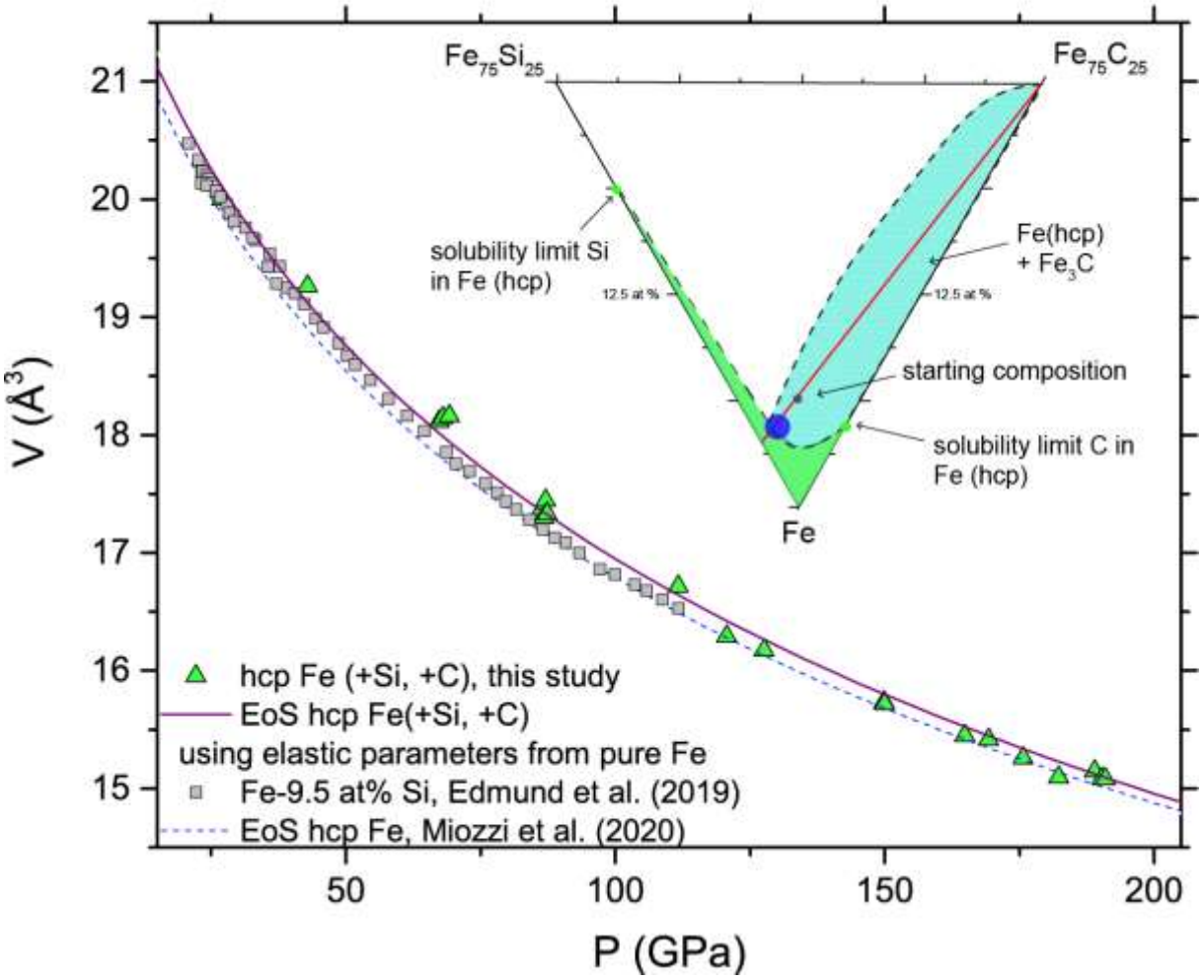

Figure 2: Plot of the molar volumes as a function of pressure at T = 300 K for C- and Si-bearing hcp Fe. Green triangles represent the experimental data from this study, purple line the EoS fitted with the elastic parameter of pure Fe, black squares the experimental data on Fe-9.5 at % Si from Edmund et al (2019). Blue dashed line the EoS of pure Fe (hcp) from (Miozzi et al. 2020). Inset: Ternary Fe-Si-C diagram showing the phase relations in the iron rich side. In red the tie line connecting the starting material and Fe_3C. In green the solubility field for Si and C in (hcp) Fe estimated at 50 GPa. The interception represents the solubility limit of light elements in iron.

At high temperature tough, a different effect seems to appear, not observed in previous calculations (Li et al., 2018), as the volumes of hcp Fe (+Si, +C) are lower than those retrieved for pure iron (Figure 3). Hcp Fe (+Si, +C) appears to have a smaller thermal expansion than pure iron. This implies that the addition of a small amount of carbon in the structure of hcp Fe, sensibly change its thermal properties. To understand to which extent and provide a quantitative evaluation, we have fitted

to our data a Vinet equation of state with a Mie Grüneisen Debye thermal model (text S1 of the Supplementary Material). We obtained the following thermal equation of state with K_0 = 143 (3) GPa, K_0' = 5.6 (1), γ_0 = 1.0 (3) and q = 4 (1) with V_0 and θ_D fixed to 6.95 cm^3/mol (= 23.065 Å^3) and 420 K respectively (Figure S2 in Supplementary Material). This offers a simple description of the thermo-elastic properties of hcp Fe (+Si, +C). However, the obtained model likely does not fully catch the complexity of the system, as highlighted by the dispersion of the experimental points with respect to the calculated isotherms and the relatively high residual pressures (± 9 GPa). The scatter in the initial data affects the quality of the obtained fit, thus compromising a reliable extrapolation of the physical properties at core's pressures. Further investigation, with improved data coverage in the examined pressure range, for both hcp Fe (+Si, +C) and pure hcp Fe is necessary to quantitatively investigate the difference in thermal expansion between the two compounds.

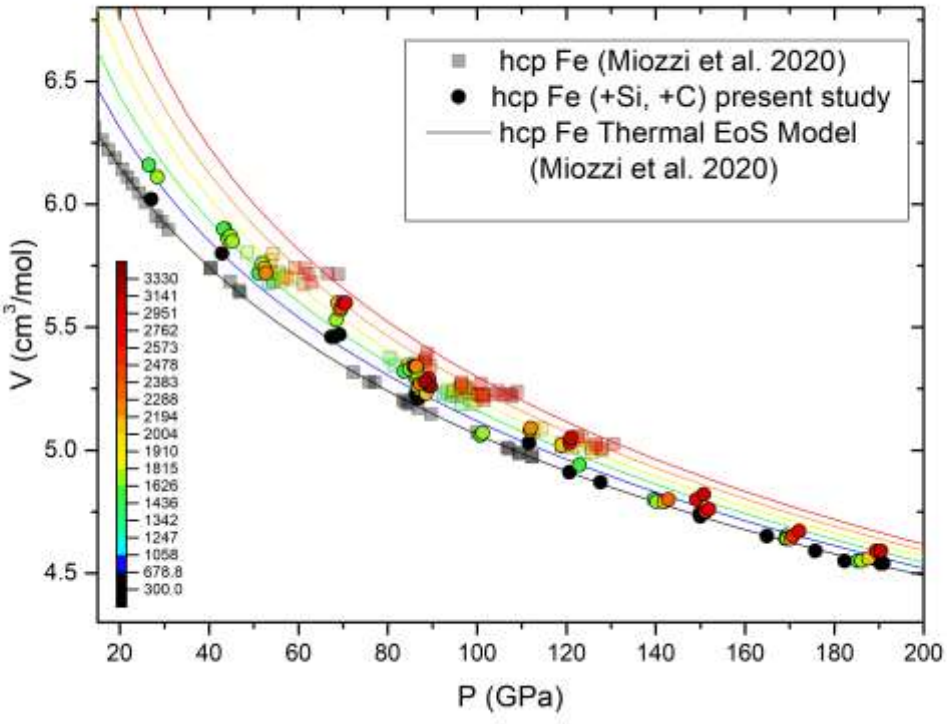

Figure 3: Plot of the volumes over pressure for hcp Fe (+Si, +C) compared with the experimental volumes of pure Fe from Miozzi et al. (2020) and its model for the thermal equation of state extrapolated for the examined pressure range.

239 Diffraction peaks of cementite (Fe_3C) were indexed based on an orthorhombic structure with
240 space group Pnma. The volumes obtained for Fe_3C as a function of pressure and temperature are shown
241 in Figure 4, together with the pressure variation of the a, b and c cell parameters at 300 K and 2000-
242 2400 K. The 300 K compression curve is consistent with previous studies in the same pressure range
243 (e.g. Sata et al., 2010) and the low-pressure trend is in good agreement with data from large volume
244 experiments (e.g. Litasov et al., 2013). While no discontinuities in the volume are visible in our dataset,
245 the cell parameters display an inversion between b and a axis at 300 K occurring between 20 and 60
246 GPa (Figure 4b). Further XRD analyses in this pressure range are needed to precisely locate the pressure
247 of transition. We suggest that the present report can be related to the one from Ono and Mibe (2010) of
248 a magnetic transition occurring around 60 GPa. However, other techniques as Mossbauer or X-ray
249 emission spectroscopy are more pertinent to further study magnetic transitions. Accordingly, we refer
250 to literature work for an extensive discussion on the topic (Gao et al., 2008; Ono and Mibe, 2010;
251 Prescher et al., 2012).

252 The P-V relation at 300 K and thermal equation of state were also refined for Fe_3C. The fit of the ambient
253 temperature data with a Vinet EoS at the 3rd order yields a V_0 = 22.65 (2) cm3/mol with K_0 = 288 (35)
254 GPa and the first pressure derivative K' = 3.7 (6). These results are consistent with the work of Sata and
255 coauthors (2010) for the non-magnetic phase. In addition, V_0 and K_0 are also comparable within the
256 error bars with those obtained employing computational methods and two different equations of state,
257 Birch Murnaghan (Vočadlo et al., 2002) and Vinet (Mookherjee, 2011). The experimentally determined
258 K' (3.7) however, is lower than the values of 4.3 in (Vočadlo et al., 2002) and 4.9 for (Mookherjee,

2011)). Once considering the entire P-T dataset, keeping the Debye temperature fixed to the values from literature (Litasov et al., 2014) and refining all the others parameters of the thermal model we obtain: V_0 = 22.63 (8) cm^3/mol, K_0 = 293 (18) GPa, K_0'= 3.6 (3), γ_0 = 3.2 (5), q = 4 (1), with the pressure residuals between ± 6 GPa and χ^2 = 1.5. The marginal difference in the values of V_0 and K_0 between the 300 K EoS and the thermal model is a consequence of the presence of numerous high temperature points between 30 and 60 GPa, which improved the fit.

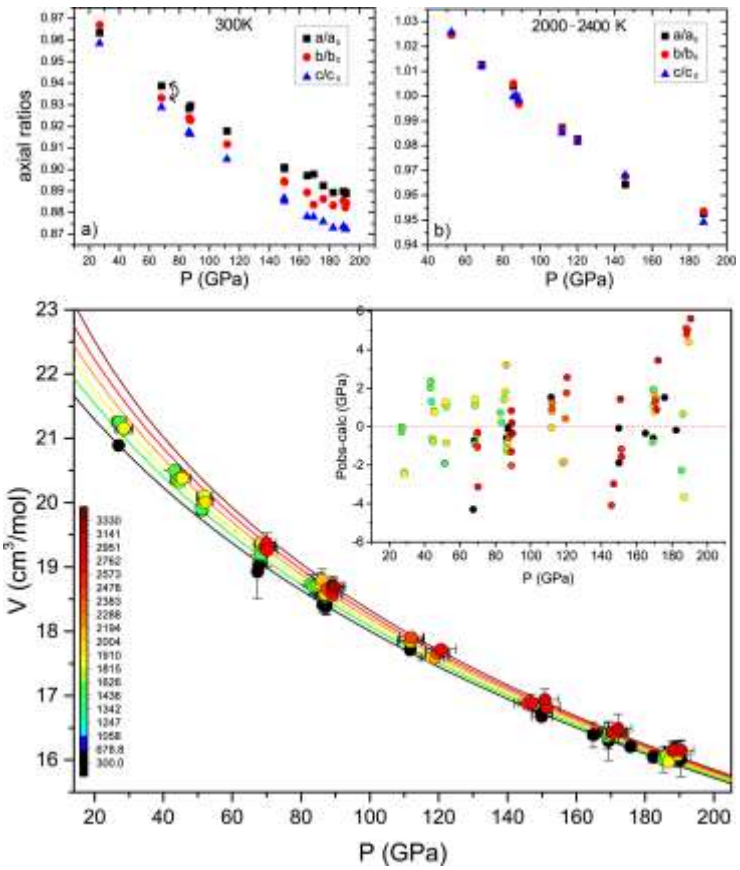

Figure 4: a) Fe_3C axial compressibility for a, b and c at 300K. b) Axial compressibility for a, b and c at high temperature. c) Experimental data (symbols) and fit with the Mie Grüneisen Debye thermal model (lines) for Fe_3C. Top right inset, pressure residuals for the fit

3.3 Melting curve

The melting relations of $FeSi_3C_4$ were measured up to 190 GPa and 3500 K (Figure 5). Over this pressure range, hcp Fe (+Si, +C) was observed in coexistence with Fe_3C before melting. Upon heating, diffraction from hcp Fe (+Si, +C) crystals is observed along with diffuse scattering from the first liquid until complete melting is reached. The obtained eutectic melting curve is lower than that observed for Fe-16wt%Si (27.5 at %) (Fischer et al., 2012) and close to the eutectic melting in the Fe-Fe_3C binary system reported by Morard et al., (2017) (Figure 5).

Silicon is known to have a negligible effect on the melting of pure Fe, conversely carbon greatly affects the melting temperatures (Morard et al., 2017). This behaviour is observed also in the ternary system where the quantity of silicon is not enough to tamper the depressing effect of carbon.

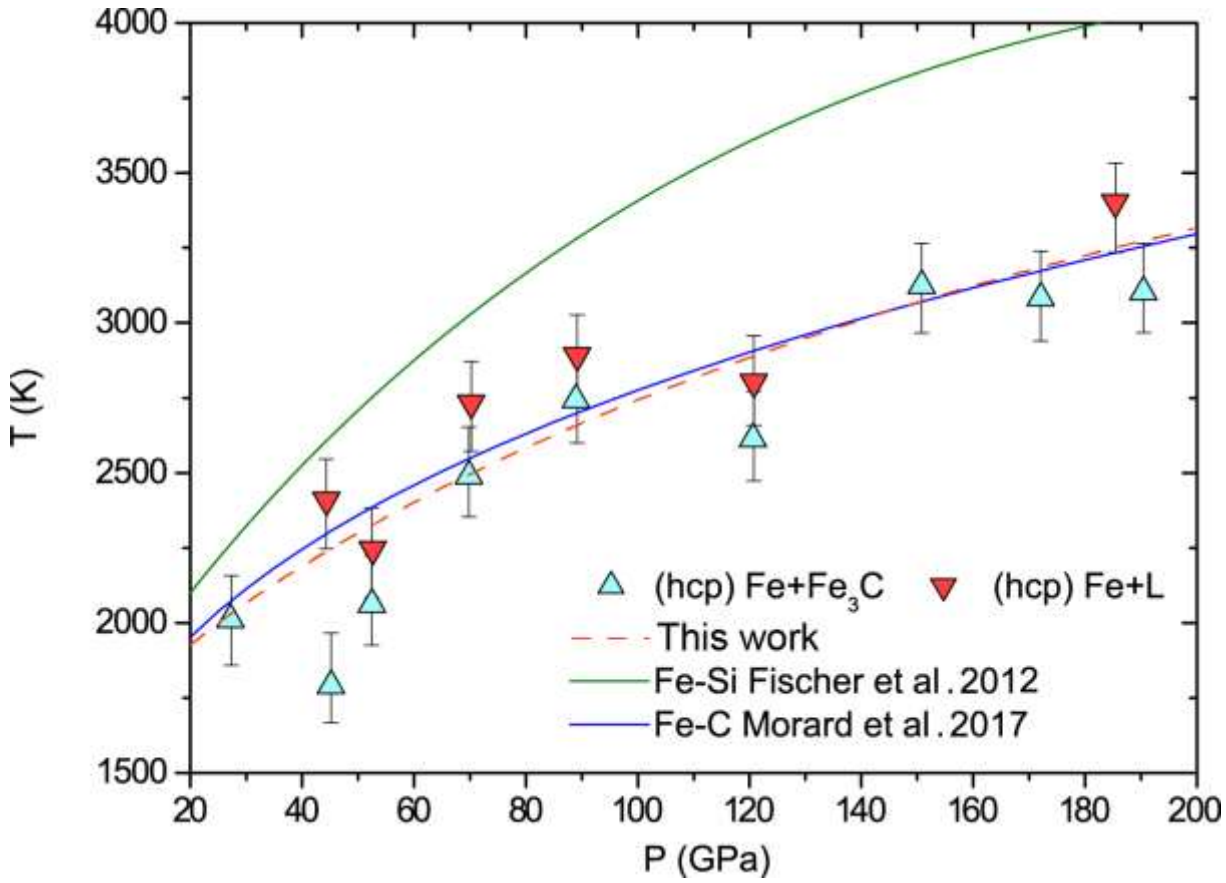

Figure 5: Eutectic melting curve for $FeSi_3C_4$. Light blue triangles facing upward represent the last P-T conditions were an assemblage (hcp) Fe (+Si, +C) + Fe_3C was stable. At the P-T conditions represented by the red facing down triangles (hcp) Fe (+Si, +C) was the only remaining solid, in equilibrium with a liquid. For comparison the melting curves of Fe-16wt%Si (Fischer et al., 2012) and eutectic melting in the Fe-Fe_3C (Morard et al., 2017) are also illustrated.

At the pressure of 50 GPa, we estimated the melt composition by Rietveld analysis of the diffraction pattern of a finely recrystallized quenched sample. The quenched sample, initially amorphous, was reheated to a temperature around 1500 K, to trigger a recrystallization without having a large elemental diffusion. Samples were kept at this temperature so to obtain sharp and continuous diffraction rings. Diffraction spots, possibly due to un-melted surrounding material were masked on the image plate, and excluded from the Rietveld intensity analysis. This approach has been already

291 successfully employed in the study of the pressure evolution of the eutectic in the binary Fe-C (Morard
292 et al, 2017) with results then independently confirmed by successive EPMA measurements (Mashino et
293 al, 2019). In the present case, it was not possible to independently confirm the Rietveld results by EPMA
294 analysis of the recovered experimental charges, since the samples that we successfully recovered from
295 the high-pressure were quickly altered in air after the FIB preparation, thus preventing any further
296 analysis.

297 A lower bound of 13 (± 4.3) at% C for the C content of the liquid in the ternary system is estimated from
298 the relative proportion of Fe_3C vs. hcp Fe (+Si, +C), neglecting the few at % C potentially present into
299 the hcp structure. As incorporation of silicon in the hcp structure of Fe does not introduce any volume
300 change, its amount could not be evaluated by Rietveld analysis. A partitioning 1:1 between solid and
301 liquid was assumed, leading to the estimate of 3 at % Si in the liquid (Fischer et al., 2015; Kuwayama
302 et al., 2009).

303 **4. Discussion**

304 From the determined melting curve, the melting relations in the Fe-rich side of the ternary
305 system can be established and used to test the hypothesis of Si and C being the major light element in
306 the Earth's core.

307 At 50 GPa the eutectic melting temperature of $FeSi_3C_4$ is ~ 2300 K, relatively close to the
308 eutectic temperature for the Fe-C binary (~ 2400 K) and well below the melting of Fe-Si binary (~ 2700
309 K from Fischer et al. 2012) systems and pure Fe (~ 2900 K from Anzellini et al. 2013 and Morard et al.,
310 2018). Carbon is known to have a strong effect on the melting of pure Fe (Morard et al., 2017) whereas
311 silicon barely affects it (Fischer et al., 2013). The measured ternary eutectic and the characteristics of
312 the two binaries enable us to determine the synthetic liquidus shape at 50 GPa (Figure 6a). At these
313 pressures Si does not affect the melting temperature, at least up to a content of 18 at%, although the
314 eutectic composition shifts toward lower silicon contents (Lord et al., 2010; Ozawa et al., 2016).
315 Conversely, carbon has a strong influence on the melting temperature while the eutectic composition is
316 constant (Mashino et al., 2019; Morard et al., 2017).

By combining the evolution in pressure of the two binary systems (Anzellini et al., 2013; Fischer et al. 2012; Morard et al., 2017) with the relationships established here for the ternary system, we can assess the ternary relations at the core mantle boundary pressure of 136 GPa (Figure 6b).

Concerning the eutectic composition, in line with the observations for the binary Fe-C (Mashino et al., 2019), a constant carbon content is assumed for the ternary system, while the silicon content is going to change with pressure, according to values reported for the Fe-FeSi binary system (Ozawa et al., 2016). Over the pressure range of interest, the melting depression in the ternary system is expected to be poorly affected by changes in the Si content, whereas carbon will be the element with stronger effect on the melting. We therefore assume that the ternary eutectic at 136 GPa qualitatively behaves as the one at 50 GPa for a similar composition, with the eutectic temperature measured at ~ 2950 K (Figure 5) and only marginally affected within +/-50 K by a moderate change in the Si content.

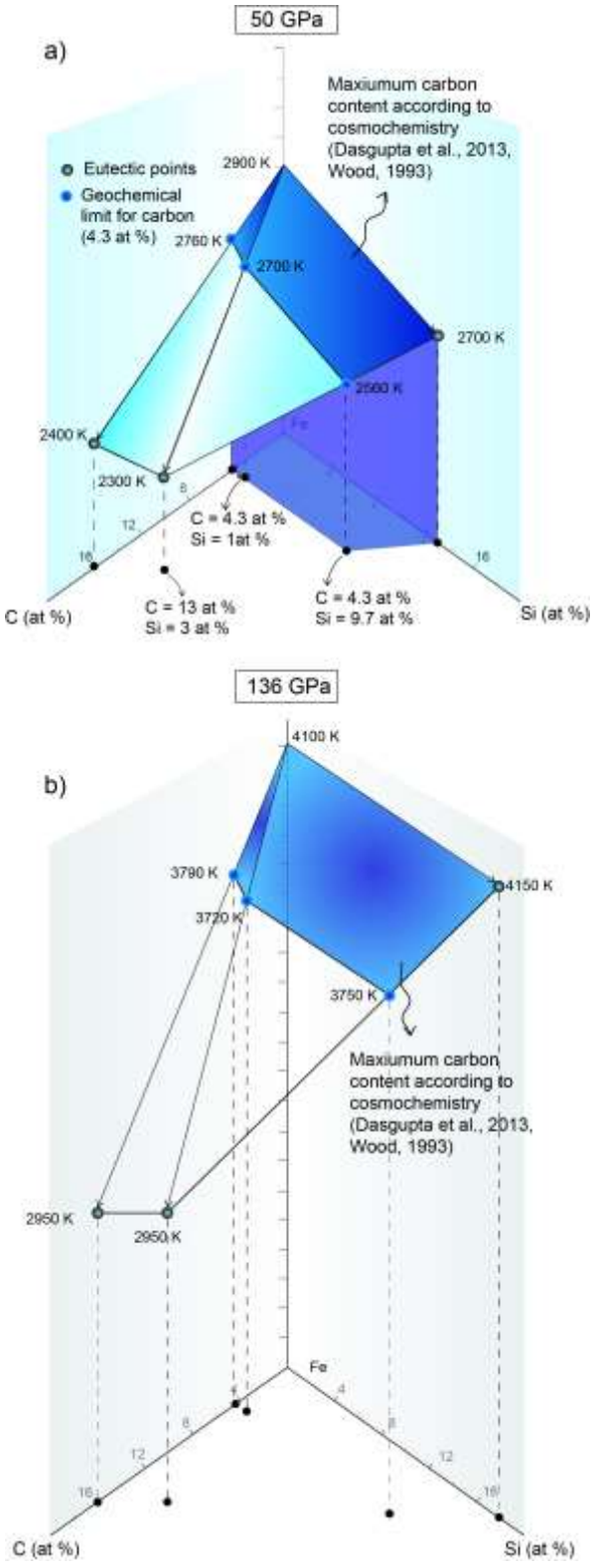

Figure 6: Surfaces representing the melting temperature in the ternary system at 50 and 136 GPa (a and b respectively). The dark blue portions stand for the compositions included within the carbon content imposed by geochemical arguments. Quantities are obtained via linear interpolation.

Additionally, to test the assumption of Si and C as the main light elements in the

Earth's core, geochemical arguments also need to be taken into account. Constraints based on silicate-metal partitioning (Dasgupta et al., 2013) limit the maximum carbon content in the Earth's core to about 1 wt % C (4.3 at % C). Estimations of silicon content span over a wider range, with the most recent models based on metal/silicate partitioning experiments ranging between 2 and 10 wt% Si (3.9 to 18 at% Si), depending upon accreting material and redox path (Siebert et al., 2013). The melting surfaces, as well as the portion of the compositional space satisfying the geochemical constraints are highlighted in Figure 6a and 6b (dark blue portions).

The melting temperature presented here can be used to discuss the temperature at the CMB for a core containing silicon and carbon as main light elements. Geotherm in the Earth's core at CMB pressure is estimated to be 400 to 900 K above the crystallisation temperature of core materials (Anzellini et al., 2013; Komabayashi, 2014). Thus, for a ternary Fe-C-Si core composition, once a constant carbon content up to 4.3 at% is assumed (dark blue region in Figure 6b), and irrespectively of the actual silicon content, temperatures at CMB would range between 4120 (±150) K and 4550 (±150) K for the lower boundary (T melt + 400 K) and 4620 (±150) K and 5050 (±150) K for the upper boundary (T melt + 900 K), shown in Figure 7a as yellow and orange surfaces. These temperature estimates are lower bounds as temperature is expected to increase if the eutectic composition had a higher carbon content. Further constraints can be placed when considering CMB from the mantle perspective. At the scale of seismological observations of the lower-most part of the mantle (> 5 km) the presence of an ubiquitous melt layer can be excluded. Indeed, even the ultra-low velocity zones (Williams and Garnero, 1996), characterized by an anomalously low shear-wave velocity, feature sometimes interpreted as due to the presence of a melt, are well-localized observations. For most of the lower mantle to be solid, the temperature at the CMB has to be lower than the solidus of the constituting material. When assuming either a chondritic or a peridotitic composition, estimated solidus temperatures at CMB range between 4100 and 4200 K (Andrault et al., 2011; Fiquet et al., 2010). The P-T-X surfaces determined in this study show that for most of the Si and C compositional range leads to temperatures laying above mantle solidus (Figure 7a), which would trigger extensive melting at the base of the mantle. There is however a narrow compositional portion for which, under the assumption of a moderate difference at CMB

pressure between core melting temperature and actual geotherm (T melt + 400 K), core temperature would remain below the 4200 K isotherm (Figure 7b and 7c). Such solution space, with a carbon content between 3.4 and 4.3 at % and maximum silicon content of 13.6 at % hence represents a core composition that would satisfy the temperature requirement. It should be noted however that both higher carbon content in the eutectic (here assumed to coincide with our lower bound estimate of 13 at %) both a difference between geotherm and crystallisation temperature of core materials at CMB pressure larger than 400 K move the estimated temperature toward higher values, above the mantle solidus for the entire compositional space.

In summary, based on our experimental results and the above discussion, we argue that there is a compositional space in the Fe-Si-C diagram that would satisfy the temperature constraints at the CMB but only under the assumptions of: i) absence of extensive mantle melting at the CMB; ii) peridotitic or chondritic lower mantle composition; and iii) core temperature at CMB not exceeding more than 400 K melting temperature of core material (lower bound to core geotherm). Within this scenario the ultra low velocity zones, could be explained as outcome of partial melting of materials more fusible than surrounding peridotitic mantle, such as mid-ocean ridge basalt (e.g. Pradhan et al., 2015). Nevertheless, we stress that the determined compositional space for carbon is narrow and shifted towards the upper geochemically acceptable limits, and that core temperature can be higher than the lower bound assumed here. As such, the presence of a third light element inducing further depression of the melting curve (i.e. oxygen, sulphur, hydrogen) still represents the most likely possibility. Finally, while the already mentioned recent calculation (Li et al., 2018) suggests Fe-C-Si alloys to have velocities compatible with PREM at inner core P-T conditions, experimental determinations support significant increase in the sound velocities of iron due Si alloying (Antonangeli et al., 2018; Edmund et al., 2019). This makes difficult to find solutions with large light element content simultaneously accounting for both velocities and density (Edmund et al., 2019), in particular when allowing for the likely presence of nickel, which increases atomic mass and reduces the thermal expansion of the alloy (Edmund et al., 2020). Further experimental work is thus necessary to confirm the theoretical predictions.

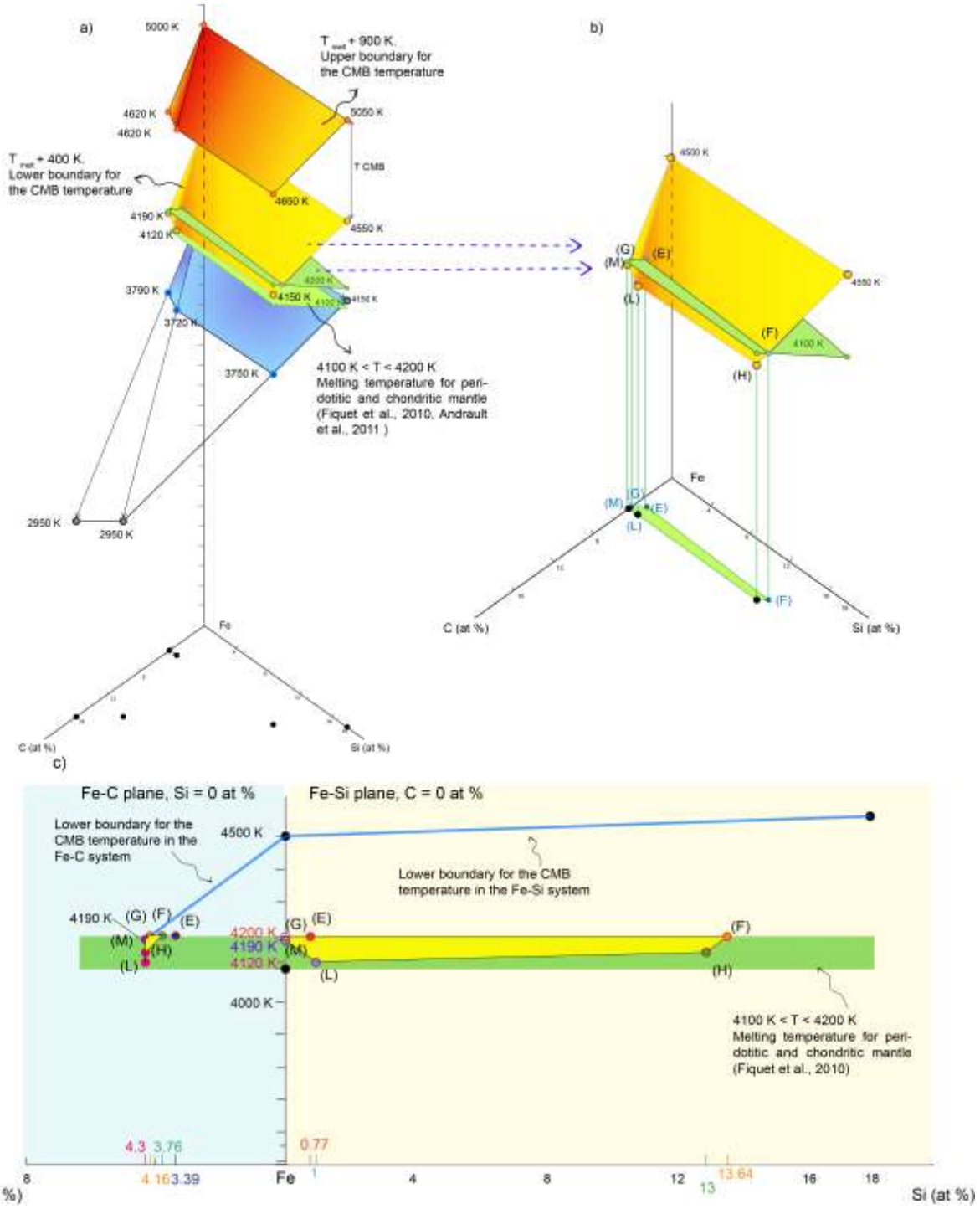

Figure 7: Extrapolation in the ternary Fe-Si-C system of the compositions that satisfy the geochemical and temperature constraints for the core. a) Yellow and orange surfaces encompass temperatures expected at the CMB for a core with a Fe-Si-C composition. In green the 4100 K and 4200 K isotherms representing the solidus of a peridotitic or chondritic mantle; b) details on the interception between the 4200 K isotherm and the compositional surface in the ternary compositional space; c) projection of the compositions on the two Fe-X-T planes. In light blue the Fe-C with 0 at % Si compositional surface and in light yellow the Fe-Si with 0 at % C compositional surface. In yellow the compositional spaces satisfying the geochemical and temperature constraints.

5. Conclusions

Phase diagram and melting curve of a Fe- 3at% Si- 4at% C ternary alloy have been investigated in a wide P-T range, using *in situ* X-ray diffraction. Our results demonstrate that, upon heating, this alloy always crystalizes in (hcp) Fe + Fe_3C, with all the silicon and part of the carbon being hosted within the iron hcp structure. Carbon in interstitial sites strongly affects the volume of hcp Fe, compared to silicon in substitution to Fe atoms. The melting curve in this ternary system is very close to the curve of the binary Fe-C system, suggesting that the effect of silicon on the melting is negligible even when carbon is added to the structure. The depression of the crystallization temperature might be sufficient to allow the presence of solid mantle at the CMB. However this condition is satisfied only for a narrow compositional range, with the carbon content close to the upper limit imposed by cosmochemical constraints, and for geotherm exceeding melting temperate by no more than 400 K at CMB. The presence of another light element seems still necessary to be taken in account if modelling a core containing silicon and carbon as the main elements alloyed with iron.

Acknowledgments

The authors wish to thank Stany Bauchau and Jeroen Jacobs (ESRF) for their help with the X-ray experiments and diamond anvil cell preparation. We also thank Imène Estève for her help with sample analysis by SEM, and Michel Fialin and Nicolas Rividi for their help during microprobe analysis. Femtosecond laser micromachining at the Institut de Minéralogie de Physique des Matériaux et de Cosmochimie (IMPMC), Paris, has been developed and realized by the "Cellule Project" with the financial support of ANR 2010-JCJC-604- 01. The Focused Ion Beam (FIB) and Scanning Electron Microscope (SEM) facility at IMPMC is supported by Région Ile de France grant SESAME 2006 N°I-07-593/R, INSU-CNRS, Institute de Physique (INP)–CNRS, University Pierre et Marie Curie–Paris 6, and by the French National Research Agency (ANR) grant ANR-07-BLAN-0124-01. This project and F. M., G. M., M.A.B. and G. F. have received funding from the European Research Council (ERC) under the European Union's Horizon 2020 research and innovation Programme (grant agreement No.

670787). D. A, and S.B. have received funding from the European Research Council (ERC) under the European Union's Horizon 2020 research and innovation Programme (grant agreement No. 724690).

References

Alfè, D., Gillan, M.., Price, G.., 2002. Composition and temperature of the Earth's core constrained by combining ab initio calculations and seismic data. Earth Planet. Sci. Lett. 195, 91–98. https://doi.org/10.1016/S0012-821X(01)00568-4

Andrault, D., Bolfan-Casanova, N., Nigro, G. Lo, Bouhifd, M.A., Garbarino, G., Mezouar, M., 2011. Solidus and liquidus profiles of chondritic mantle: Implication for melting of the Earth across its history. Earth Planet. Sci. Lett. 304, 251–259. https://doi.org/10.1016/j.epsl.2011.02.006

Antonangeli, D., Morard, G., Paolasini, L., Garbarino, G., Murphy, C.A., Edmund, E., Decremps, F., Fiquet, G., Bosak, A., Mezouar, M., Fei, Y., 2018. Sound velocities and density measurements of solid hcp-Fe and hcp-Fe–Si (9 wt.%) alloy at high pressure: Constraints on the Si abundance in the Earth's inner core. Earth Planet. Sci. Lett. 482, 446–453. https://doi.org/10.1016/j.epsl.2017.11.043

Antonangeli, D., Siebert, J., Badro, J., Farber, D.L., Fiquet, G., Morard, G., Ryerson, F.J., 2010. Composition of the Earth's inner core from high-pressure sound velocity measurements in Fe–Ni–Si alloys. Earth Planet. Sci. Lett. 295, 292–296. https://doi.org/10.1016/j.epsl.2010.04.018

Anzellini, S., Dewaele, A., Mezouar, M., Loubeyre, P., Morard, G., 2013. Melting of Iron at Earth's Inner Core Boundary Based on Fast X-ray Diffraction. Science (80-.). 340, 464–466. https://doi.org/10.1126/science.1233514

Birch, F., 1964. Density and composition of mantle and core. J. Geophys. Res. 69, 4377–4388. https://doi.org/10.1029/JZ069i020p04377

Boehler, R., De Hantsetters, K., 2004. New anvil designs in diamond-cells. High Press. Res. 24, 391–396. https://doi.org/10.1080/08957950412331323924

Campbell, A.J., Danielson, L., Righter, K., Seagle, C.T., Wang, Y., Prakapenka, V.B., 2009. High pressure effects on the iron-iron oxide and nickel-nickel oxide oxygen fugacity buffers. Earth Planet. Sci. Lett. 286, 556–564. https://doi.org/10.1016/j.epsl.2009.07.022

Caracas, R., 2017. The influence of carbon on the seismic properties of solid iron. Geophys. Res. Lett. 44, 128–134. https://doi.org/10.1002/2016GL071109

Chabot, N.L., Campbell, A.J., Jones, J.H., Humayun, M., Vern Lauer, H., 2006. The influence of carbon on trace element partitioning behavior. Geochim. Cosmochim. Acta 70, 1322–1335. https://doi.org/10.1016/j.gca.2005.11.011

Dasgupta, R., 2013. Ingassing, Storage, and Outgassing of Terrestrial Carbon through Geologic Time. Rev. Mineral. Geochemistry 75, 183–229. https://doi.org/10.2138/rmg.2013.75.7

Dasgupta, R., Chi, H., Shimizu, N., Buono, A.S., Walker, D., 2013. Carbon solution and partitioning between metallic and silicate melts in a shallow magma ocean: Implications for the origin and distribution of terrestrial carbon. Geochim. Cosmochim. Acta 102, 191–212. https://doi.org/10.1016/j.gca.2012.10.011

Dewaele, A., Belonoshko, A.B., Garbarino, G., Occelli, F., Bouvier, P., Hanfland, M., Mezouar, M., 2012. High-pressure–high-temperature equation of state of KCl and KBr. Phys. Rev. B 85, 214105. https://doi.org/10.1103/PhysRevB.85.214105

Dewaele, A., Loubeyre, P., Occelli, F., Mezouar, M., Dorogokupets, P.I., Torrent, M., 2006. Quasihydrostatic Equation of State of Iron above 2 Mbar. Phys. Rev. Lett. 97, 215504. https://doi.org/10.1103/PhysRevLett.97.215504

Dziewonski, A.M., Anderson, D.L., 1981. Preliminary reference Earth model. Phys. Earth Planet. Inter. 25, 297–356. https://doi.org/10.1016/0031-9201(81)90046-7

Edmund, E., Antonangeli, D., Decremps, F., Miozzi, F., Morard, G., Boulard, E., Clark, A.N., Ayrinhac, S., Gauthier, M., Morand, M., Mezouar, M., 2019. Velocity-Density Systematics of Fe-5wt%Si: Constraints on Si Content in the Earth's Inner Core. J. Geophys. Res. Solid Earth 124, 3436–3447. https://doi.org/10.1029/2018JB016904

484 Edmund, E., Miozzi, F., Morard, G., Boulard, E., Clark, A., Decremps, F., Garbarino, G., Svitlyk, V.,
485 Mezouar, M., Antonangeli, D., 2020. Axial Compressibility and Thermal Equation of State of
486 Hcp Fe–5wt% Ni–5wt% Si. Minerals 10, 98. https://doi.org/10.3390/min10020098
487 Fei, Y., Murphy, C., Shibazaki, Y., Shahar, A., Huang, H., 2016. Thermal equation of state of hcp-
488 iron: Constraint on the density deficit of Earth's solid inner core. Geophys. Res. Lett. 43, 6837–
489 6843. https://doi.org/10.1002/2016GL069456
490 Fiquet, G., Auzende, A.L., Siebert, J., Corgne, A., Bureau, H., Ozawa, H., Garbarino, G., 2010.
491 Melting of peridotite to 140 gigapascals. Science (80-.). 329, 1516–1518.
492 https://doi.org/10.1126/science.1192448
493 Fischer, R.A., Campbell, A.J., Caracas, R., Reaman, D.M., Dera, P., Prakapenka, V.B., 2012. Equation
494 of state and phase diagram of Fe–16Si alloy as a candidate component of Earth's core. Earth
495 Planet. Sci. Lett. 357–358, 268–276. https://doi.org/10.1016/j.epsl.2012.09.022
496 Fischer, R.A., Campbell, A.J., Reaman, D.M., Miller, N.A., Heinz, D.L., Dera, P., Prakapenka, V.B.,
497 2013. Phase relations in the Fe-FeSi system at high pressures and temperatures. Earth Planet. Sci.
498 Lett. 373, 54–64. https://doi.org/10.1016/j.epsl.2013.04.035
499 Fischer, R.A., Nakajima, Y., Campbell, A.J., Frost, D.J., Harries, D., Langenhorst, F., Miyajima, N.,
500 Pollok, K., Rubie, D.C., 2015. High pressure metal-silicate partitioning of Ni, Co, V, Cr, Si, and
501 O. Geochim. Cosmochim. Acta 167, 177–194. https://doi.org/10.1016/j.gca.2015.06.026
502 Gao, L., Chen, B., Wang, J., Alp, E.E., Zhao, J., Lerche, M., Sturhahn, W., Scott, H.P., Huang, F.,
503 Ding, Y., Sinogeikin, S. V., Lundstrom, C.C., Bass, J.D., Li, J., 2008. Pressure-induced magnetic
504 transition and sound velocities of Fe 3 C: Implications for carbon in the Earth's inner core.
505 Geophys. Res. Lett. 35, L17306. https://doi.org/10.1029/2008GL034817
506 Hirose, K., Morard, G., Sinmyo, R., Umemoto, K., Hernlund, J., Helffrich, G., Labrosse, S., 2017.
507 Crystallization of silicon dioxide and compositional evolution of the Earth's core. Nature 543,
508 99–102. https://doi.org/10.1038/nature21367
509 Javoy, M., Kaminski, E., Guyot, F., Andrault, D., Sanloup, C., Moreira, M., Labrosse, S., Jambon, A.,
510 Agrinier, P., Davaille, A., Jaupart, C., 2010. The chemical composition of the Earth: Enstatite
511 chondrite models. Earth Planet. Sci. Lett. 293, 259–268.
512 https://doi.org/10.1016/j.epsl.2010.02.033
513 Komabayashi, T., 2014. Thermodynamics of melting relations in the system Fe-FeO at high pressure:
514 Implications for oxygen in the Earth's core. J. Geophys. Res. Solid Earth 119, 4164–4177.
515 https://doi.org/10.1002/2014JB010980
516 Kuwayama, Y., Sawai, T., Hirose, K., Sata, N., Ohishi, Y., 2009. Phase relations of iron-silicon alloys
517 at high pressure and high temperature. Phys. Chem. Miner. 36, 511–518.
518 https://doi.org/10.1007/s00269-009-0296-0
519 Li, Y., Vočadlo, L., Brodholt, J.P., 2018. The elastic properties of hcp -Fe alloys under the conditions
520 of the Earth's inner core. Earth Planet. Sci. Lett. 493, 118–127.
521 https://doi.org/10.1016/j.epsl.2018.04.013
522 Liermann, H.P., Konôpková, Z., Morgenroth, W., Glazyrin, K., Bednarčik, J., McBride, E.E.,
523 Petitgirard, S., Delitz, J.T., Wendt, M., Bican, Y., Ehnes, A., Schwark, I., Rothkirch, A., Tischer,
524 M., Heuer, J., Schulte-Schrepping, H., Kracht, T., Franz, H., 2015. The Extreme Conditions
525 Beamline P02.2 and the Extreme Conditions Science Infrastructure at PETRA III. J. Synchrotron
526 Radiat. 22, 908–924. https://doi.org/10.1107/S1600577515005937
527 Litasov, K.D., Sharygin, I.S., Dorogokupets, P.I., Shatskiy, A., Gavryushkin, P.N., Sokolova, T.S.,
528 Ohtani, E., Li, J., Funakoshi, K., 2013. Thermal equation of state and thermodynamic properties
529 of iron carbide Fe3C to 31 GPa and 1473 K. J. Geophys. Res. Solid Earth 118, 5274–5284.
530 https://doi.org/10.1002/2013JB010270
531 Litasov, K.D., Sharygin, I.S., Shatskii, a. F., Gavryushkin, P.N., Dorogokupets, P.I., Sokolova, T.S.,
532 Ohtani, E., Dymshits, a. M., Alifirova, T. a., 2014. P-V-T equations of state for iron carbides
533 Fe3C and Fe7C3 and their relationships under the conditions of the Earth's mantle and core.
534 Dokl. Earth Sci. 453, 1269–1273. https://doi.org/10.1134/S1028334X13120192
535 Liu, J., Lin, J.F., Prakapenka, V.B., Prescher, C., Yoshino, T., 2016. Phase relations of Fe3C and
536 Fe7C3up to 185 GPa and 5200 K: Implication for the stability of iron carbide in the Earth's core.
537 Geophys. Res. Lett. 43, 12,415-12,422. https://doi.org/10.1002/2016GL071353
538 Lord, O.T., Walter, M.J., Dobson, D.P., Armstrong, L., Clark, S.M., Kleppe, A., 2010. The FeSi phase

539 diagram to 150 GPa. J. Geophys. Res. Solid Earth 115, 1–9.
540 https://doi.org/10.1029/2009JB006528
541 Mashino, I., Miozzi, F., Hirose, K., Morard, G., Sinmyo, R., 2019. Melting experiments on the Fe–C
542 binary system up to 255 GPa: Constraints on the carbon content in the Earth's core. Earth Planet.
543 Sci. Lett. 515, 135–144. https://doi.org/10.1016/j.epsl.2019.03.020
544 McDonough, W.F., 2003. Compositional Model for the Earth's Core, in: Treatise on Geochemistry.
545 Elsevier, pp. 547–568. https://doi.org/10.1016/B0-08-043751-6/02015-6
546 Mezouar, M., Crichton, W.A., Bauchau, S., Thurel, F., Witsch, H., Torrecillas, F., Blattmann, G.,
547 Marion, P., Dabin, Y., Chavanne, J., Hignette, O., Morawe, C., Borel, C., 2005. Development of
548 a new state-of-the-art beamline optimized for monochromatic single-crystal and powder X-ray
549 diffraction under extreme conditions at the ESRF. J. Synchrotron Radiat. 12, 659–664.
550 https://doi.org/10.1107/S0909049505023216
551 Miozzi, F., Morard, G., Antonangeli, D., Clark, A.N., Mezouar, M., Dorn, C., Rozel, A., Fiquet, G.,
552 2018. Equation of State of SiC at Extreme Conditions: New Insight Into the Interior of Carbon-
553 Rich Exoplanets. J. Geophys. Res. Planets 19, 2295–2309.
554 https://doi.org/10.1029/2018JE005582
555 Miozzi, Matas, Guignot, Badro, Siebert, Fiquet, 2020. A New Reference for the Thermal Equation of
556 State of Iron. Minerals 10, 100. https://doi.org/10.3390/min10020100
557 Mookherjee, M., 2011. Elasticity and anisotropy of Fe3C at high pressures. Am. Mineral. 96, 1530–
558 1536. https://doi.org/10.2138/am.2011.3917
559 Morard, G., Andrault, D., Antonangeli, D., Nakajima, Y., Auzende, A.L., Boulard, E., Cervera, S.,
560 Clark, A., Lord, O.T., Siebert, J., Svitlyk, V., Garbarino, G., Mezouar, M., 2017. Fe–FeO and
561 Fe–Fe3C melting relations at Earth's core–mantle boundary conditions: Implications for a
562 volatile-rich or oxygen-rich core. Earth Planet. Sci. Lett. 473, 94–103.
563 https://doi.org/10.1016/j.epsl.2017.05.024
564 Morard, G., Andrault, D., Guignot, N., Siebert, J., Garbarino, G., Antonangeli, D., 2011. Melting of
565 Fe-Ni-Si and Fe-Ni-S alloys at megabar pressures: Implications for the core-mantle boundary
566 temperature. Phys. Chem. Miner. 38, 767–776. https://doi.org/10.1007/s00269-011-0449-9
567 Morard, G., Boccato, S., Rosa, A.D., Anzellini, S., Miozzi, F., Henry, L., Garbarino, G., Mezouar, M.,
568 Harmand, M., Guyot, F., Boulard, E., Kantor, I., Irifune, T., Torchio, R., 2018. Solving
569 Controversies on the Iron Phase Diagram Under High Pressure. Geophys. Res. Lett. 45, 11,074-
570 11,082. https://doi.org/10.1029/2018GL079950
571 Narumi, T., Kawanishi, S., Yoshikawa, T., Kusunoki, K., Kamei, K., Daikoku, H., Sakamoto, H.,
572 2014. Thermodynamic evaluation of the C–Cr–Si, C–Ti–Si, and C–Fe–Si systems for rapid
573 solution growth of SiC. J. Cryst. Growth 408, 25–31.
574 https://doi.org/10.1016/j.jcrysgro.2014.08.027
575 Ono, S., Mibe, K., 2010. Magnetic transition of iron carbide at high pressures. Phys. Earth Planet.
576 Inter. 180, 1–6. https://doi.org/10.1016/j.pepi.2010.03.008
577 Ozawa, H., Hirose, K., Yonemitsu, K., Ohishi, Y., 2016. High-pressure melting experiments on Fe-Si
578 alloys and implications for silicon as a light element in the core. Earth Planet. Sci. Lett. 456, 47–
579 54. https://doi.org/10.1016/j.epsl.2016.08.042
580 Poirier, J., 1994. Light elements in the Earth's outer core: A critical review. Phys. Earth Planet. Inter.
581 85, 319–337. https://doi.org/10.1016/0031-9201(94)90120-1
582 Pradhan, G.K., Fiquet, G., Siebert, J., Auzende, A.-L., Morard, G., Antonangeli, D., Garbarino, G.,
583 2015. Melting of MORB at core–mantle boundary. Earth Planet. Sci. Lett. 431, 247–255.
584 https://doi.org/10.1016/j.epsl.2015.09.034
585 Prescher, C., Dubrovinsky, L., Bykova, E., Kupenko, I., Glazyrin, K., Kantor, A., McCammon, C.,
586 Mookherjee, M., Nakajima, Y., Miyajima, N., Sinmyo, R., Cerantola, V., Dubrovinskaia, N.,
587 Prakapenka, V., Rüffer, R., Chumakov, A., Hanfland, M., 2015. High Poisson's ratio of Earth's
588 inner core explained by carbon alloying. Nat. Geosci. 8, 220–223.
589 https://doi.org/10.1038/ngeo2370
590 Prescher, C., Dubrovinsky, L., McCammon, C., Glazyrin, K., Nakajima, Y., Kantor, A., Merlini, M.,
591 Hanfland, M., 2012. Structurally hidden magnetic transitions in Fe 3C at high pressures. Phys.
592 Rev. B - Condens. Matter Mater. Phys. 85, 6–9. https://doi.org/10.1103/PhysRevB.85.140402
593 Prescher, C., Prakapenka, V.B., 2015. DIOPTAS: a program for reduction of two-dimensional X-ray

diffraction data and data exploration. High Press. Res. 35, 223–230. https://doi.org/10.1080/08957959.2015.1059835
Sata, N., Hirose, K., Shen, G., Nakajima, Y., Ohishi, Y., Hirao, N., 2010. Compression of FeSi, Fe<inf>3</inf>C, Fe<inf>0.95</inf>O, and FeS under the core pressures and implication for light element in the Earth's core. J. Geophys. Res. Solid Earth 115, 1–13. https://doi.org/10.1029/2009JB006975
Siebert, J., Badro, J., Antonangeli, D., Ryerson, F.J., 2013. Terrestrial Accretion Under Oxidizing Conditions. Science (80-.). 339, 1194–1197. https://doi.org/10.1126/science.1227923
Tateno, S., Hirose, K., Synmio, R., Morard, G., Hirao, N., Ohishi, Y., 2018. Melting experiments on Fe – Si – S alloys to core pressures : Silicon in the core ? Am. Mineral. 103, 742–748.
Tateno, S., Kuwayama, Y., Hirose, K., Ohishi, Y., 2015. The structure of Fe-Si alloy in Earth's inner core. Earth Planet. Sci. Lett. 418, 11–19. https://doi.org/10.1016/j.epsl.2015.02.008
Vočadlo, L., Brodholt, J.P., Dobson, D.P., Knight, K.S., Marshall, W.G., Price, G.D., Wood, I.G., 2002. The effect of ferromagnetism on the equation of state of Fe 3 C studied by first-principles calculations. Earth Planet. Sci. Lett. 203, 567–575.
Vočadlo, L., Poirer, J.P., Price, G.D., 2000. Gruneisen parameters and isothermal equations of state. Am. Mineral. 85, 390–395. https://doi.org/10.2138/am-2000-2-319
Williams, Q., Garnero, E.J., 1996. Seismic Evidence for Partial Melt at the Base of Earth's Mantle. Science (80-.). 273, 1528–1530. https://doi.org/10.1126/science.273.5281.1528
Wood, B.J., 1993. Carbon in the core. Earth Planet. Sci. Lett. 117, 593–607. https://doi.org/10.1016/0012-821X(93)90105-I
Wood, B.J., Li, J., Shahar, A., 2013. Carbon in the Core: Its Influence on the Properties of Core and Mantle. Carbon in Earth 75, 231–250. https://doi.org/10.2138/rmg.2013.75.8

619

620

621

Supplementary material for:

"**Eutectic melting of Fe-3 at% Si-4at% C alloy up to 200 GPa and implications for the Earth's core**."

Figure S1: Diffraction patterns collected for increasing temperature in a heating run. The presence of a diffuse scattering signal identifies the melting.

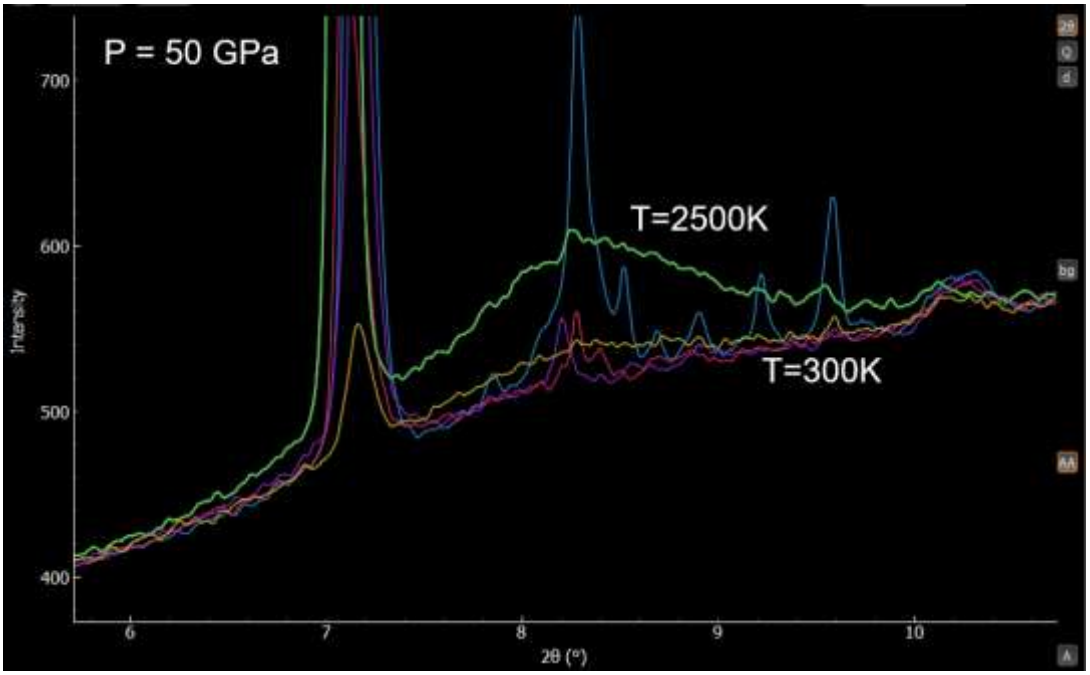

Text S1: Details on the equation of state and thermal model formalism.

The PVT data sets obtained for both hcp Fe (+Si, +C) and Fe_3C were fitted with a 3rd order Vinet equation of state to describe the isothermal compression, plus a thermal pressure component following the Mie Grüneisen Debye thermal model.

Isothermal pressure is defined as:

$$P=3K_0 \frac{(1-f_V)}{f_V^2} \exp\left(\frac{3}{2}\left(K_0'-1\right)(1-f_V)\right)$$

where $f_V = \left(\frac{V}{V_0}\right)^{\frac{1}{3}}$, v the volume at pressure and v_0 that at ambient conditions.

For the thermal model the Mie Grüneisen Debye parametrization was used in which the pressure at high temperature is consider as resulting from the sum of the pressure at a reference temperature (here ambient T) and the thermal pressure. The thermal pressure can be written as a function of the vibrational energy E, the Gruneisen parameter γ and the volume:

$$P_{th} = \frac{\gamma(V)}{V} [E(T,\theta_D)-E_c(T_c, \theta_D)]$$

In turn, the lattice vibrational energy is expressed as a function of the temperature T normalized to the characteristic Debye temperature θ_D and written as:

$$E(T,\theta_D)=9nRT\left(\frac{T}{\theta_D}\right)^3 \int_0^{\frac{\theta_D}{T}} \frac{t^3 dt}{e^t-1}$$

where n is the number of atoms per formula unit, R is the gas constant. The Debye temperature

$$\theta_D = \theta_0 \exp\left[\frac{\left(\gamma_0 - \gamma(V)\right)}{q}\right]$$

is a function of the Debye temperature at reference conditions (θ_0) and the Grüneisen parameter (γ) given by

$$\gamma(V) = \gamma_0 \left(\frac{V}{V_0}\right)^q$$

where q corresponds to the logarithmic volume dependence of γ(V).

More details regarding the used equations of state are available for example in (Jackson and Rigden, 1996; Milani et al., 2017). All the refinement were performed with the EoSFit suite (Angel et al., 2014).

Due to the difficulties encountered in refining V_0 from the experimental data, in the present study V_0 was calculated by adding to the V_0 of pure Fe from Miozzi et al. (2020) a delta V obtained averaging the difference between the experimental volumes of hcp Fe (+Si, +C) and those of pure Fe over the

pressure range of interest. For the same reason the Debye temperature was kept fixed to the value of pure Fe (i.e. 420 K) (e.g. Edmund et al., 2019; Fei et al., 2016).

Figure S2. Right: Experimental data interpolated with the isotherms recalculated from the obtained thermal equation of state. The ambient temperature data have been fitted with a 3rd order Vinet EoS and a Mie Grüneisen Debye formalism has been employed for the thermal data. Left: Plot of the residuals on pressure versus the observed pressures.

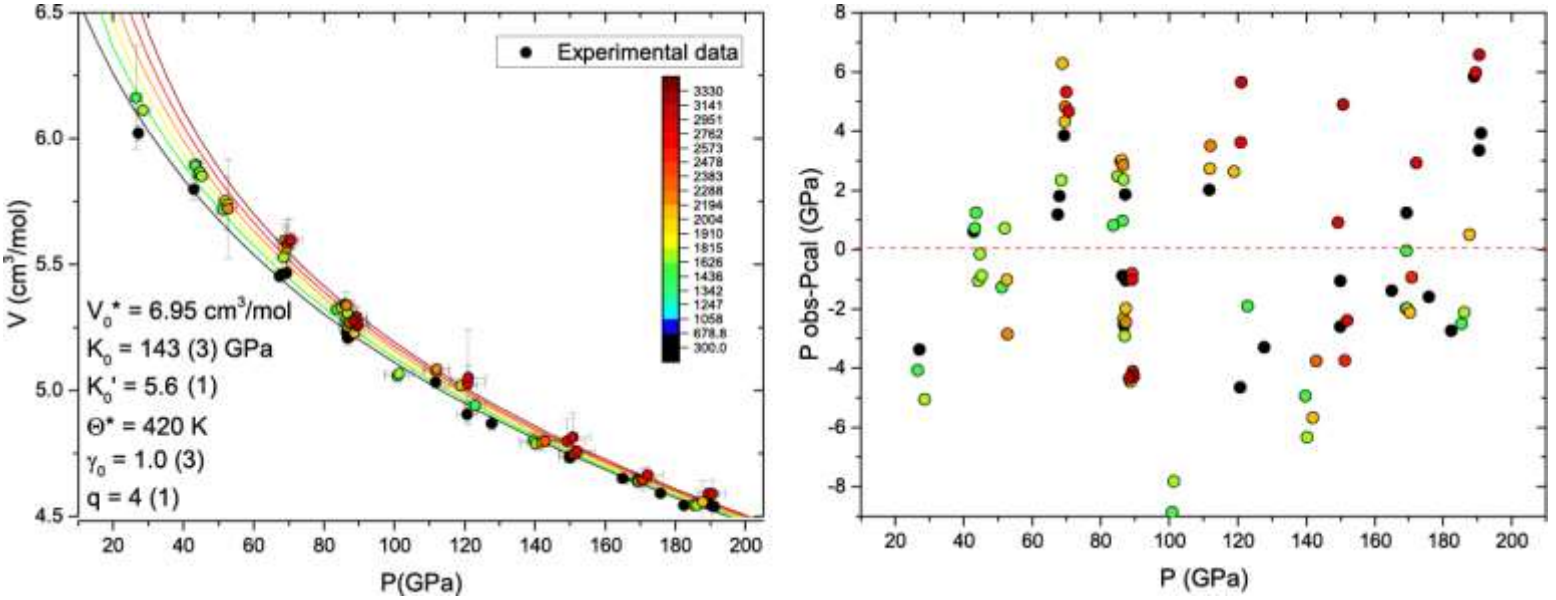

Figures S3-S5: Diffraction patterns fitted with GSAS. Listed reflections are those used for the fit in PDIndexer.

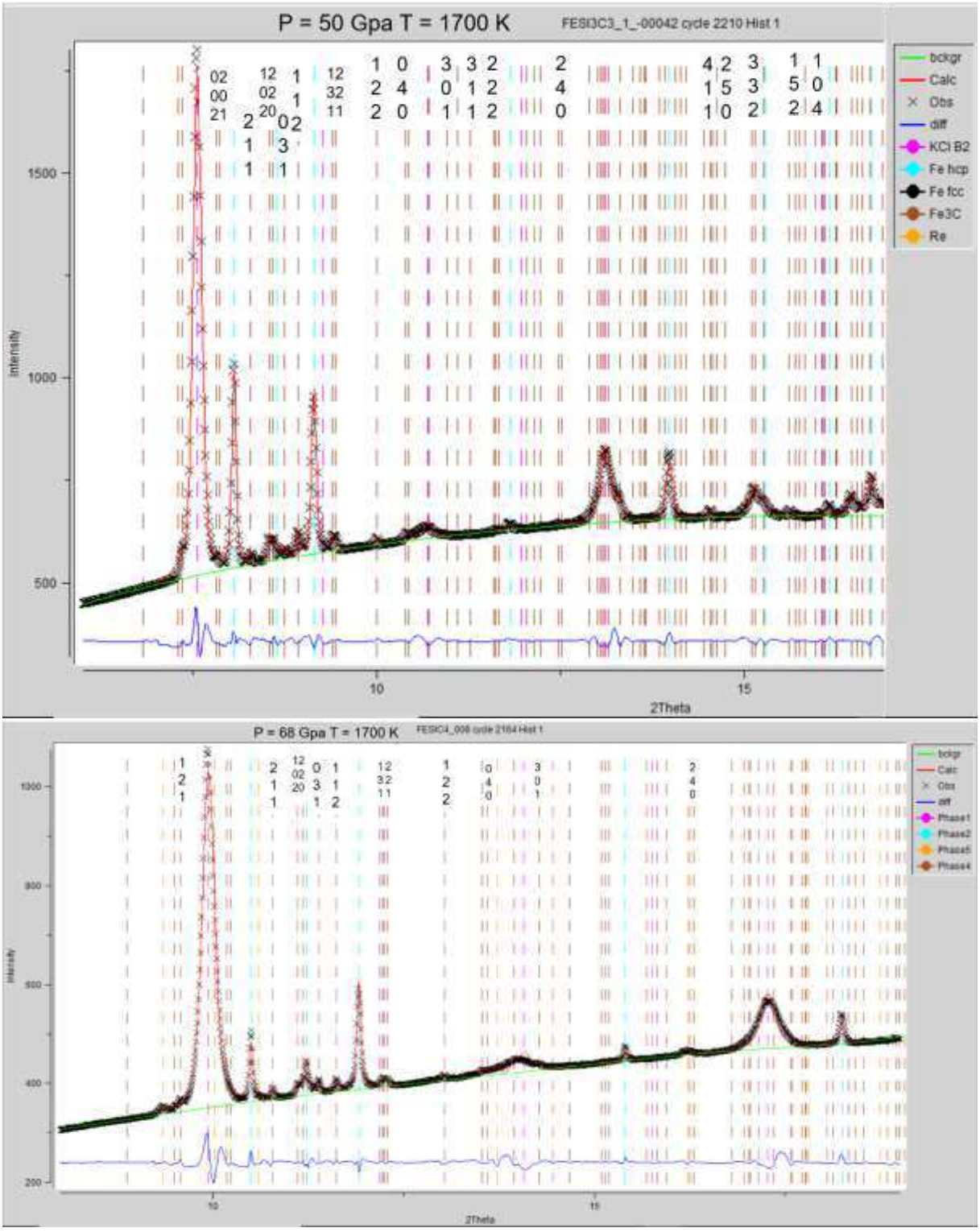

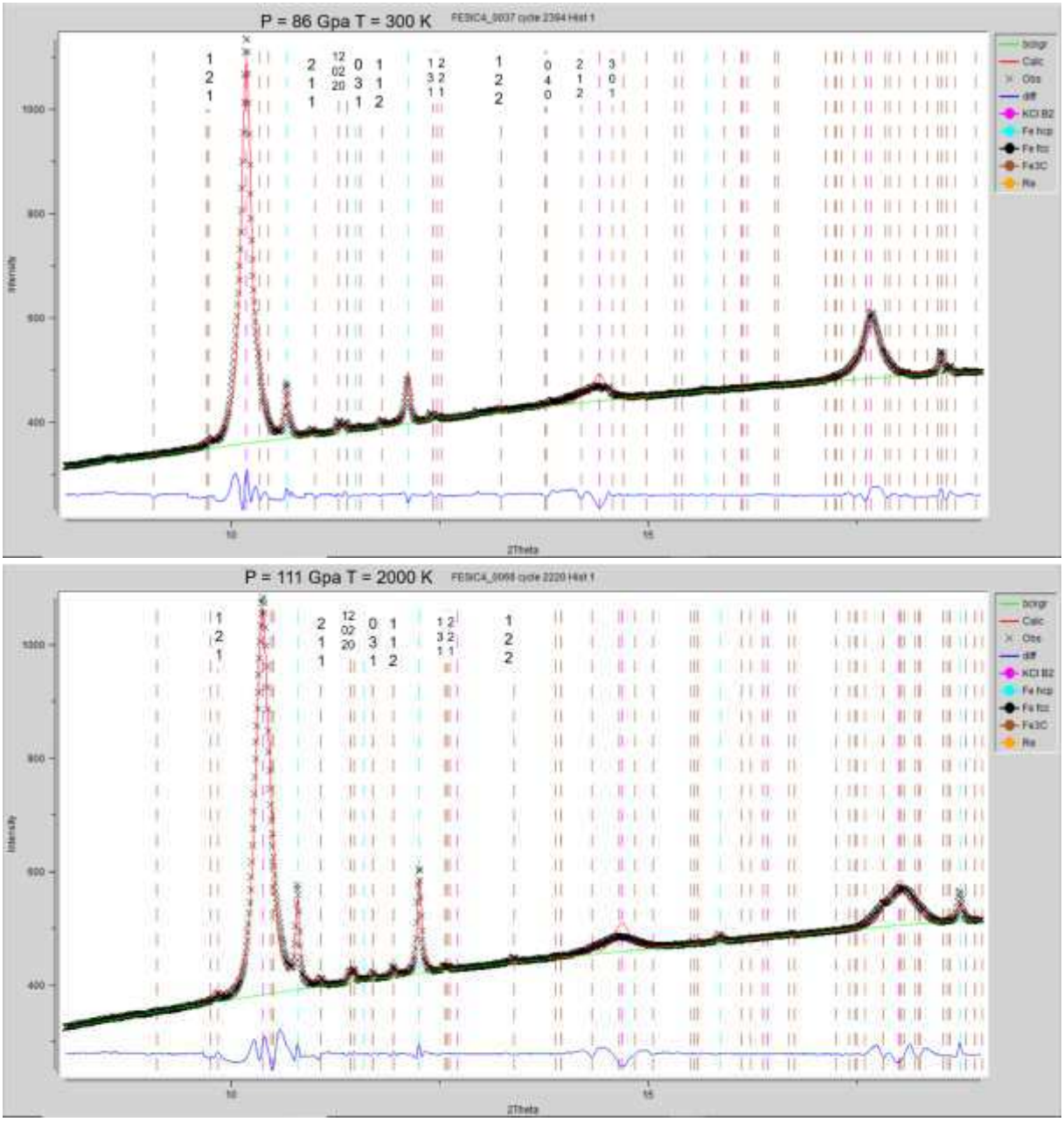

References

Angel, R.J., Gonzalez-Platas, J., Alvaro, M., 2014. EosFit7c and a Fortran module (library) for equation of state calculations. Zeitschrift fur Krist. 229, 405–419. https://doi.org/10.1515/zkri-2013-1711

Edmund, E., Antonangeli, D., Decremps, F., Miozzi, F., Morard, G., Boulard, E., Clark, A.N., Ayrinhac, S., Gauthier, M., Morand, M., Mezouar, M., 2019. Velocity-Density Systematics of Fe-5wt%Si: Constraints on Si Content in the Earth's Inner Core. J. Geophys. Res. Solid Earth 124, 3436–3447. https://doi.org/10.1029/2018JB016904

Fei, Y., Murphy, C., Shibazaki, Y., Shahar, A., Huang, H., 2016. Thermal equation of state of hcp-iron: Constraint on the density deficit of Earth's solid inner core. Geophys. Res. Lett. 43, 6837–6843. https://doi.org/10.1002/2016GL069456

Jackson, I., Rigden, S.M., 1996. Analysis of P-V-T data: constraints on the thermoelastic properties of

high-pressure minerals. Phys. Earth Planet. Inter. 96, 85–112. https://doi.org/10.1016/0031-9201(96)03143-3

Milani, S., Angel, R.J., Scandolo, L., Mazzucchelli, M.L., Ballaran, T.B., Klemme, S., Domeneghetti, M.C., Miletich, R., Scheidl, K.S., Derzsi, M., Tokár, K., Prencipe, M., Alvaro, M., Nestola, F., 2017. Thermo-elastic behavior of grossular garnet at high pressures and temperatures. Am. Mineral. 102, 851–859. https://doi.org/10.2138/am-2017-5855

Fe(hcp) in FeSi3C4

P GPa T K V cm^3/mol

Format 1 P sigP T sigT V sigV

27.02	0.27	300.00	3.00	6.02	0.03
42.91	0.53	300.00	3.00	5.80	0.04
67.37	0.52	300.00	3.00	5.46	0.02
67.98	2.08	300.00	3.00	5.46	0.01
69.21	0.25	300.00	3.00	5.47	0.03
86.35	0.18	300.00	3.00	5.23	0.02
86.73	0.17	300.00	3.00	5.21	0.03
87.08	0.23	300.00	3.00	5.25	0.03
87.22	0.22	300.00	3.00	5.22	0.02
87.35	0.29	300.00	3.00	5.22	0.02
111.67	0.86	300.00	3.00	5.03	0.02
120.68	2.99	300.00	3.00	4.91	0.03
127.67	1.66	300.00	3.00	4.87	0.03
149.86	3.00	300.00	3.00	4.74	0.02
149.96	3.00	300.00	3.00	4.73	0.02
164.9	1.55	300.00	3.00	4.65	0.01
188.94	0.30	300.00	3.00	4.56	0.01
169.33	0.28	300.00	3.00	4.64	0.01
175.74	0.41	300.00	3.00	4.59	0.01
182.32	0.68	300.00	3.00	4.55	0.01
190.39	1.01	300.00	3.00	4.54	0.06
190.98	0.52	300.00	3.00	4.54	0.02
185.26	2.70	1505.00	150.00	4.55	0.02
86.37	2.34	1507.70	150.00	5.29	0.01
51.11	1.68	1515.30	150.00	5.72	0.01
100.82	3.63	1520.00	150.00	5.06	0.02
139.64	4.00	1520.00	150.00	4.80	0.03
43.52	1.59	1536.00	150.00	5.90	0.01
83.63	1.80	1559.50	150.00	5.32	0.01
169.26	3.81	1560.70	150.00	4.65	0.03
122.89	3.00	1562.00	150.00	4.94	0.03
169.1	3.07	1562.00	150.00	4.64	0.02
26.51	1.65	1570.00	150.00	6.16	0.20
43.24	1.80	1588.80	150.00	5.90	0.02
186.1	2.44	1700.70	150.00	4.55	0.01
86.99	2.75	1703.50	150.00	5.25	0.03
140.25	4.00	1703.70	150.00	4.79	0.03
169.45	3.21	1704.00	150.00	4.64	0.02
84.9	1.79	1707.50	150.00	5.33	0.01
101.3	3.97	1716.00	150.00	5.07	0.01
44.17	1.05	1717.00	150.00	5.86	0.02
86.66	2.28	1720.00	150.00	5.26	0.04
68.46	2.08	1723.00	150.00	5.53	0.01
86.66	2.53	1724.30	150.00	5.31	0.01
28.46	2.26	1744.00	150.00	6.11	0.02
44.73	1.80	1759.50	150.00	5.87	0.03
51.85	1.99	1782.80	150.00	5.76	0.01
45.22	1.78	1791.80	150.00	5.85	0.02
87.22	2.48	2059.00	150.00	5.27	0.04
52.52	2.47	2062.80	150.00	5.74	0.10
88.63	2.73	2065.00	150.00	5.23	0.03
85.78	2.26	2066.30	150.00	5.34	0.02
68.8	2.26	2067.30	150.00	5.60	0.06

141.89	4.00	2071.30	150.00	4.79	0.03
187.68	2.24	2088.00	150.00	4.56	0.08
111.89	3.53	2098.20	150.00	5.08	0.01
170.28	3.94	2101.00	150.00	4.64	0.02
118.88	4.50	2105.00	150.00	5.02	0.02
86.1	2.42	2140.50	150.00	5.34	0.05
69.4	2.39	2187.00	150.00	5.57	0.08
87.28	2.44	2210.00	150.00	5.27	0.04
52.68	2.64	2243.80	150.00	5.72	0.20
112.06	3.60	2269.00	150.00	5.09	0.01
86.42	2.42	2282.50	150.00	5.34	0.02
69.61	2.52	2288.80	150.00	5.58	0.09
142.88	4.00	2294.50	150.00	4.80	0.02
151.19	4.47	2502.30	150.00	4.75	0.02
170.7	3.84	2520.30	150.00	4.65	0.04
89.16	2.87	2550.00	150.00	5.28	0.05
69.96	2.79	2588.50	150.00	5.60	0.09
120.79	5.00	2801.50	150.00	5.03	0.08
151.94	5.00	2876.00	150.00	4.76	0.02
89.21	2.95	2890.00	150.00	5.29	0.05
70.57	3.13	2900.00	150.00	5.60	0.03
149.17	5.00	2901.70	150.00	4.80	0.09
189.41	3.13	2912.00	150.00	4.59	0.02
172.1	4.41	2922.20	150.00	4.67	0.03
121	5.00	2979.00	150.00	5.05	0.19
89.34	3.13	3019.50	150.00	5.26	0.04
190.45	3.69	3104.00	150.00	4.59	0.05
150.78	5.00	3125.00	150.00	4.82	0.10
89.62	3.37	3153.00	150.00	5.26	0.04
88.3	3.50	3322.00	150.00	5.28	0.03

Fe3C in FeSi3C4

P GPa T K V cm^3/mol

Format 1 P sigP T sigT V sigV

27.02	0.27	300.0	3	20.89273	0.00151
67.37	0.52	300.0	3	18.92984	0.41709
67.98	2.08	300.0	3	19.03855	0.10917
86.35	0.18	300.0	3	18.4093	0.12076
87.35	0.29	300.0	3	18.39454	0.14365
87.22	0.22	300.0	3	18.3956	0.12347
111.67	0.86	300.0	3	17.71425	0.05586
149.86	3.00	300.0	3	16.72286	0.03569
149.96	3.00	300.0	3	16.6804	0.0774
164.9	1.55	300.0	3	16.39295	0.19861
169.33	0.28	300.0	3	16.29658	0.29769
175.74	0.41	300.0	3	16.21	0.07423
182.32	0.68	300.0	3	16.04813	0.08989
188.94	0.30	300.0	3	16.10294	0.25944
190.98	0.52	300.0	3	16.04738	0.23866
190.39	1.01	300.0	3	16.01546	0.28173
43.8	1.57	1418.3	150	20.38876	0.01506
51.23	1.59	1431.5	150	19.88057	0.01506
68.39	1.82	1448.0	150	19.20117	0.06098
26.84	1.92	1449.0	150	21.25773	0.01506
27.24	1.90	1486.0	150	21.26089	0.01506
82.75	1.79	1494.8	150	18.73379	0.14877
185.26	2.70	1505.0	150	16.01124	0.20358
51.11	1.68	1515.3	150	19.90346	0.01506
43.52	1.59	1536.0	150	20.4901	0.00151
83.63	1.80	1559.5	150	18.69404	0.12528
169.26	3.81	1560.7	150	16.42261	0.08282
169.1	3.07	1562.0	150	16.36841	0.20448
43.24	1.80	1588.8	150	20.50214	0.01506
186.1	2.44	1700.7	150	16.06259	0.01506
86.99	2.28	1703.5	150	18.54497	0.01686
169.45	3.21	1704.0	150	16.41012	0.07152
84.9	1.79	1707.5	150	18.71331	0.1703
44.17	2.05	1717.0	150	20.35217	0.01506
86.66	2.28	1720.0	150	18.56499	0.00858
68.46	2.08	1723.0	150	19.32766	0.00873
86.66	2.53	1724.3	150	18.57614	0.02168
28.46	2.26	1744.0	150	21.13516	0.01506
44.73	1.80	1759.5	150	20.32687	0.01506
51.85	1.99	1782.8	150	20.07647	0.01506
45.22	1.78	1791.8	150	20.39222	0.01506
52.2	1.77	1801.3	150	20.05779	0.01506
45.45	2.48	1825.0	150	20.38499	0.01506
28.45	2.65	1830.0	150	21.16076	0.01506
117.93	3.73	1841.5	150	17.59273	0.06761
87.1	2.40	1881.0	150	18.58502	0.00783
51.9	2.26	1889.0	150	20.10598	0.01506
186.78	2.20	1893.5	150	15.97616	0.01009
170.04	3.65	1899.5	150	16.40259	0.02349
68.58	2.25	1905.5	150	19.37147	0.03794
85.69	2.10	1919.5	150	18.73108	0.18084
189.43	3.59	1980.0	150	16.08608	0.19921
111.74	3.43	1980.7	150	17.83606	0.01144

52.17	2.37	1981.0	150	20.01398	0.01506
111.94	3.83	1996.3	150	17.85639	0.0128
170.28	3.94	2101.0	150	16.42849	0.06535
118.88	4.00	2105.0	150	17.59439	0.08809
86.1	2.42	2140.5	150	18.80049	0.16684
69.4	2.39	2187.0	150	19.3135	0.09697
170.45	3.87	2303.3	150	16.43029	0.04818
119.61	3.60	2305.0	150	17.65703	0.06113
187.87	2.51	2338.8	150	16.15158	0.14726
112.12	3.49	2348.0	150	17.90397	0.03222
69.71	2.59	2389.0	150	19.31531	0.09878
87.34	2.56	2412.5	150	18.66121	0.03358
89.03	2.77	2451.5	150	18.55641	0.06505
112.04	3.31	2459.4	150	17.90939	0.02921
188.24	2.66	2487.5	150	16.14631	0.11489
69.9	2.70	2491.3	150	19.32449	0.09757
145.74	3.70	2495.3	150	16.87961	0.06761
120.28	2.47	2496.0	150	17.69557	0.06339
151.19	4.00	2502.3	150	16.82058	0.03222
170.7	3.84	2520.3	150	16.44113	0.06716
89.16	2.87	2550.0	150	18.62432	0.14877
69.96	2.79	2588.5	150	19.37283	0.0786
120.66	4.50	2615.0	150	17.72072	0.03132
89.08	2.81	2650.0	150	18.60881	0.00708
70.14	2.91	2669.2	150	19.26291	0.26426
146.99	3.68	2691.3	150	16.89165	0.13416
188.65	2.84	2699.5	150	16.15459	0.12016
151.39	3.70	2709.0	150	16.82224	0.07363
171.31	3.92	2719.5	150	16.43029	0.06339
88.99	2.82	2745.0	150	18.70217	0.09019
89.34	3.13	3019.5	150	18.70894	0.15374
172.08	3.98	3085.2	150	16.49293	0.22406
190.45	3.69	3104.0	150	16.15354	0.15735
150.78	4.17	3125.0	150	16.94044	0.16277
89.62	3.37	3153.0	150	18.69946	0.11549